The use of computer simulation in the evaluation of electric vehicle batteries

W.B. Gu [a], C.Y. Wang [a, *], B.Y. Liaw [b]

[a] *Department of Mechanical Engineering and Pennsylvania Transportation Institute, The Pennsylvania State University, University Park, PA 16802, USA*
[b] *Hawaii Natural Energy Institute, SOEST, University of Hawaii at Manoa, Honolulu, HI 96822, USA*

Abstract

An integrated simulation and testing approach is presented to evaluate batteries for electric vehicle (EV) applications. This new approach combines traditional experimental testing with computer simulations to create a cost-effective means to evaluate EV batteries and provide important information that is difficult or impossible to obtain from purely experimental measurements. The present simulators for the lead–acid and nickel–metal hydride (Ni–MH) batteries are developed based on the fundamental principles governing their electrochemical behaviors and are created using an advanced computational fluid dynamics (CFD) technique. Computer simulations are validated by experimental data under the dynamic stress test (DST) procedure for a lead–acid battery module and a Ni–MH cell with good agreement. Moreover, computer simulations reveal that the studied lead–acid battery underutilizes the active material by as much as 70% and the MH electrode of the Ni–MH cell is overdesigned by about 30% under the simulated EV duty. Therefore, there is good potential of increasing the specific energy and reducing the cost if batteries are optimized for EVs using a simulation-based design approach. © 1998 Elsevier Science S.A. All rights reserved.

Keywords: Electric vehicle batteries; Dynamic testing; Computer simulation

1. Introduction

One way to improve air quality in urban areas is to replace conventional internal-combustion (IC)-engine automobiles with electric vehicles (EV) powered by rechargeable batteries. However, the success of such a replacement depends greatly on the development of advanced batteries for EV use. Requirements for EV batteries include: (1) a high specific energy for a driving range comparable to that of a conventional IC-engine powered vehicle; (2) a high specific power for accelerating and hill-climbing capabilities; and (3) a long cycle life to assure an acceptable cost. The performance of an EV is mainly controlled by the performance of its battery system; hence, the evaluation of battery performance becomes essential in the development of EVs.

Traditionally, the evaluation of EV batteries relies on experimental testing at both laboratory and field scales. For example, to estimate the driving range of an EV, one can use the peak power vs. depth of discharge (DOD) plot and the specific energy vs. specific power plot (Ragone plot), provided the power vs. speed relationship for the vehicle is known [1]. However, creating these plots involves a range of constant-current and constant-power discharge tests and, thus, is time-consuming and costly.

Various test schemes have been developed that aim at providing a direct measure of the battery performance in an EV environment. Among them, the Simplified Federal Urban Driving Schedule (SFUDS) [2] and the Dynamic Stress Test (DST) [3] are two power-based test procedures to evaluating the power delivering capability of EV batteries [4–8]. The difference between the DST and SFUDS lies in that the DST is defined by the percentage of the peak power vs. time, while the SFUDS employs the specific power with the maximum of 79 W/kg vs. time (see Fig. 1).

The facility needed to implement these test schemes for EV batteries is a computer-controlled battery cycler capable of controlling various modes of charge and discharge regimes on the battery. Since the simulated driving cycles
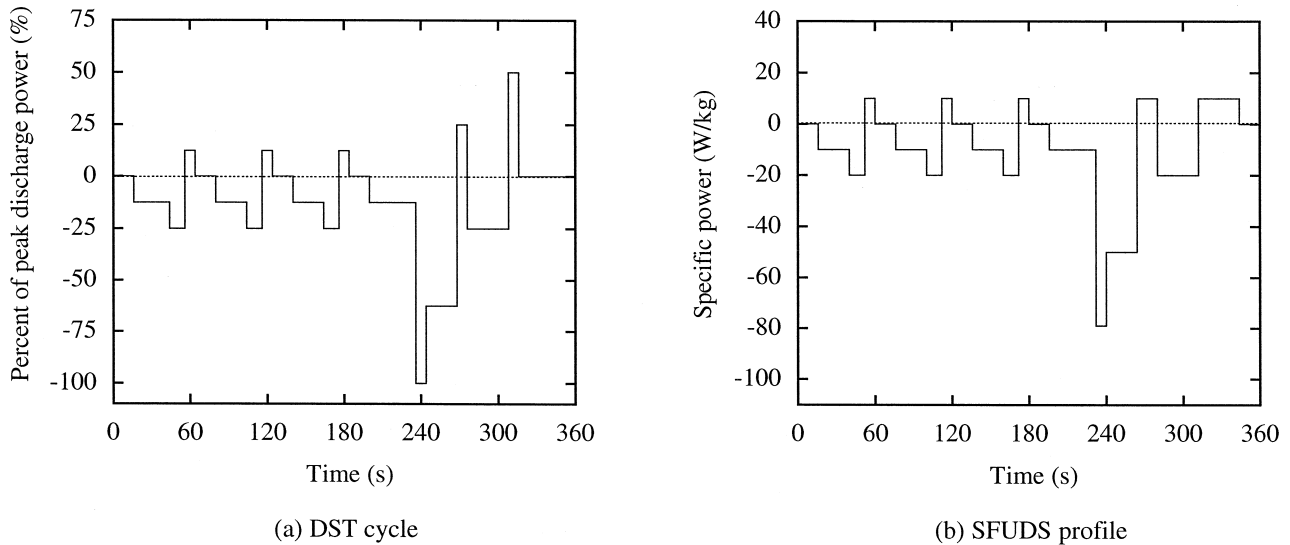
* Corresponding author. E-mail: cxw31@psu.edu

Fig. 1. DST cycle and SFUDS profile.

like DST and SFUDS are characterized by high power loads and short pulses, and the power as a product of current and voltage is usually measured only indirectly, accurate laboratory testing requires sophisticated equipment [8]. In some circumstances, an EV battery may not be comprehensively tested due to the insufficient power resolution or limitation of the battery cycler [1]. Moreover, purely experimental testing does not enable innovative design and optimization of batteries.

To overcome the above-mentioned limitations in battery testing, the alternative approach of assessing EV battery performance by a numerical modeling has been recognized for a long time [9]. A numerical simulator based on the first principles cannot only help to improve the understanding of underlying mechanisms by which batteries work, but also provide internal information that is difficult to obtain even from experiments of state-of-the-art. Such information is particularly valuable for the design and optimization of battery systems. For instance, acid depletion in lead–acid batteries and solid-state diffusion in nickel–metal hydride (Ni–MH) batteries are usually the limiting factors of battery performance, but it is difficult to measure them in situ. On the other hand, they can be easily computed from simulations provided battery simulators are fully validated by experimental data.

Attempts were made to use mathematical models to evaluate battery performance under simulated driving cycles [9–13]. Tiedemann and Newman [9] numerically investigated the thermal response of a lead–acid battery under a simulated driving cycle similar to SAE J227 a/D (a current-based test procedure). Ekdunge [10] simulated the RWE-driving cycle (also a current-based test procedure) using a simplified mathematical model for lead–acid batteries which treats the battery as three separate regions (i.e., the positive electrode, the separator, and the negative electrode) and calculates electrode potentials empirically in

each region to significantly reduce computational time. Chen and Evans [11] numerically studied the thermal behavior of a lithium–polymer battery under the SFUDS profile. They employed empirical equations for the electrochemical reaction rate. Doyle and Newman [12] outlined a mathematical approach to evaluating the limitations of lithium–polymer battery systems but did not give simulation results for driving cycles. Most recently, Karden et al. [13] presented a mathematical model for a valve-regulated lead–acid battery based on fundamental principles. Their simulations were made for a highly dynamic current-based discharge cycle.

In this article, we present a new approach to evaluate EV batteries by integrating computer simulation into experimental testing. While experimental testing is able to provide battery performance data (e.g., peak power and capacity) under simulated driving cycles, computer simulations can, in addition to validating these performance data, provide information that is difficult or impossible to obtain from experimental measurements. Integration of the two thus promises a cost-effective but comprehensive approach to evaluating EV batteries.

Section 2 presents numerical simulators for lead–acid and Ni–MH batteries, respectively, based on the fundamental principles of thermodynamics, electrochemistry, species transport, solid-state diffusion, and charge transfer [14–17]. These first-principle models are numerically solved using a Computational Fluid Dynamics (CFD) technique. Boundary conditions in terms of power as required in both DST and SFUDS profiles can be directly implemented in the present simulators, a unique feature different from virtually all previous codes where current-based conditions are required and simulating power boundary conditions requires iterations. Section 3 briefly describes the traditional experimental testing conducted in a laboratory. Section 4 demonstrates the use of these CFD battery codes,

in conjunction with the laboratory testing, for the evaluation of two EV batteries under the standard procedure. Conclusions and areas of future research are summarized in Section 5.

2. Computer simulation

2.1. Description of cell models

A battery module is composed of cells connected in series and in parallel to satisfy the requirement of voltage and capacity. The battery modeling therefore rests on the cell modeling for the fundamental phenomena of electrochemistry and species transport. A general micro-macroscopic model for batteries and fuel cells based on these first principles was recently developed by Wang et al. [16], which not only incorporates species and charge conservation in the solid matrix and electrolyte phase, respectively, but also accounts for the interfacial phenomena occurring at the electrode/electrolyte interface. The model equations were derived based on the concentrated electrolyte theory and the volume-averaging approach. These equations address such physico-chemical phenomena as: (1) electrochemical reactions via the Butler–Volmer equation; (2) transport of species in each phase due to diffusion, migration, and/or convection; (3) potential drop across either electronic- and/or ionic-conducting phase; and (4) local changes in electrode structures. Applications of the general model to lead–acid, Ni–Cd and Ni–MH batteries were demonstrated in the previous work [14–17], and model predictions were compared with a number of previous theoretical and experimental results available in the literature.

In the present work, focus is placed on lead–acid and Ni–MH batteries as they are chosen to represent a wide array of EV batteries for demonstration of the unique capabilities offered by the integrated simulation and testing approach.

There are vast differences in the operating mechanisms between lead–acid and Ni–MH batteries. While lead–acid batteries undergo a solid phase transformation during the electrochemical reaction, Ni–MH batteries involve the solid-state diffusion of hydrogen in the MH particles and the diffusion of protons in the solid Ni electrode. Moreover, the acid is consumed during discharge and reproduced during charge at both positive and negative electrodes in the lead–acid cell. Hence, acid depletion is usually a limiting factor of cell discharge, and the transport of acid from the reservoir and/or separator into the porous electrode is key to a successful cell operation. In contrast, the alkaline solution serving as the electrolyte in the Ni–MH cell is overall conserved during a cell operation, and the cell performance is, instead, limited by the species diffusion in the solid phase. The diffusion coefficients of active materials at both electrodes are therefore important

parameters dictating the performance of intercalative battery. More details of the cell models for lead–acid and Ni–MH batteries can be found in Refs. [14–17] and, thus, are not repeated here.

2.2. Battery models

Construction of a battery model from a single cell electrochemical model is necessary in order to develop a simulator for EV battery modules. Battery modeling can be readily accomplished by considering the battery configuration consisting of cells connected in series and in parallel as well as accounting for the electrical resistances contributed by intercell connectors, terminals, and cell grids, as schematically shown in Fig. 2. Let V, I, and R denote the voltage, current, and electrical resistance, with subscripts b and c referring to battery and cell, respectively. The battery voltage can then be expressed in terms of the cell voltage as follows:

$$V_b = N_s V_c + I_b \left((N_s - 1) R_{ic} + 2 R_t + \frac{2 N_s R_g}{N_p} \right) \quad (1)$$

where N stands for the number of cells, with subscripts s and p denoting cells in series and in parallel, respectively. The current through the whole battery, I_b, is related to the cell current simply by:

$$I_b = N_p I_c \quad (2)$$

Various electrical resistances appearing in Eq. (1) are schematically illustrated in Fig. 2. While the intercell resistance R_{ic} and the terminal resistance R_t can be measured, the resistance of cell grids, R_g, is geometry-dependent and usually can only be estimated from battery test data [18].

Using Eqs. (1) and (2), and noting that power is the product of current and voltage, the cell power is then related to the battery power by:

$$P_c = \frac{P_b}{N_p N_s} - \left[\frac{N_p}{N_s} \left((N_s - 1) R_{ic} + 2 R_t + \frac{2 N_s R_g}{N_p} \right) \right] I_c^2$$

$$= C_1 - C_2 I_c^2 \quad (3)$$

where:

$$C_1 = \frac{P_b}{N_p N_s} \quad (4)$$

and:

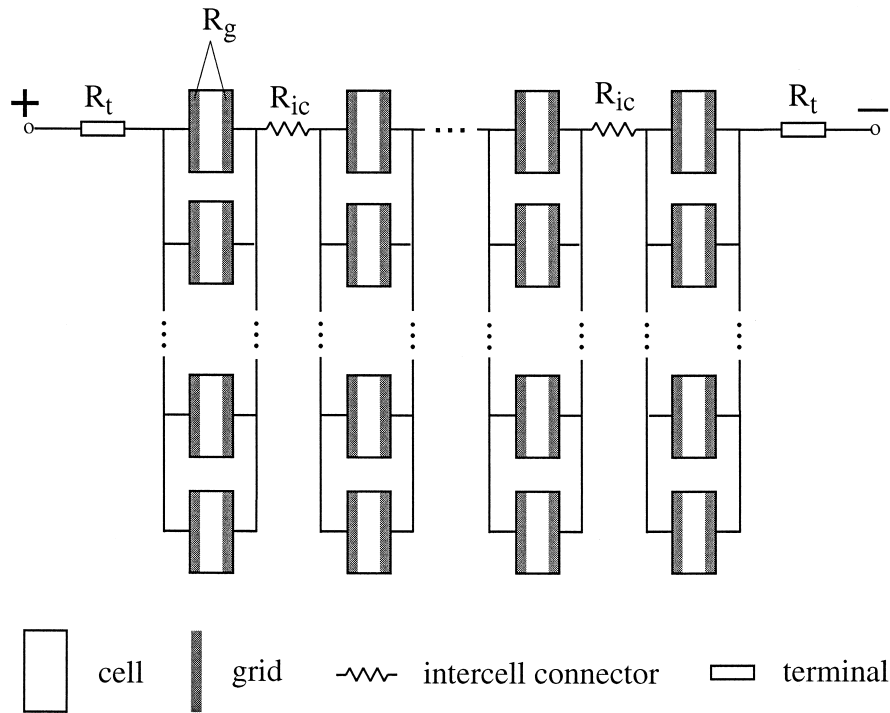$$C_2 = \frac{N_p}{N_s} \left((N_s - 1) R_{ic} + 2 R_t + \frac{2 N_s R_g}{N_p} \right) \quad (5)$$

Fig. 2. Schematic configuration of a battery module.

When the power applied to the battery, P_b, is given, C_1 and C_2 become constant. Eq. (3) thus provides a link between the cell model and the module simulator. In other words, given the power profile for the battery and various internal resistances, coefficients C_1 and C_2 can be computed via Eqs. (4) and (5), and Eq. (3) then represents a boundary condition for the cell model.

2.3. Challenge to simulate driving cycles

The boundary condition for the cell model, Eq. (3), represents a numerical difficulty and requires a special treatment, since the battery current and voltage are not known a priori. Most previous models in the literature are based on the multiregion approach, that is, the governing equations are formulated and solved separately in the positive electrode, separator, and negative electrode. The solution for the whole cell is obtained by requiring a common current density across each interface between two distinct regions. Such a solution methodology is convenient when the current density is prescribed, but necessarily calls for iterations in cases where the boundary condition is not current-based.

The second numerical difficulty arises from the highly dynamic characteristics of driving cycles. The battery current changes direction in seconds so that a small time step is needed for a sufficient temporal resolution in order to obtain convergent solutions. These features make the dynamic simulation of driving cycles much more time-consuming than that for a single constant-current charge or discharge.

2.4. Numerical procedures

To overcome the above-mentioned numerical difficulties, we employ an advanced CFD technique, in which the model equations are written in the following general form

$$\underbrace{\frac{\partial \Phi}{\partial t}}_{\text{transient}} + \underbrace{\nabla \cdot (v\Phi)}_{\text{convection}} = \underbrace{\nabla \cdot (\Gamma \nabla \Phi)}_{\text{diffusion}} + \underbrace{S}_{\text{source}} \qquad (6)$$

where Φ stands for a general variable to be solved and can represent species concentration, potential, phase fraction, and so on, in a battery model. Γ is a diffusion coefficient and S a source term which includes all terms that cannot be included in the previous terms. Some examples of S-term can be found in Ref. [14] for lead–acid batteries.

The initial condition is set in terms of the initial state of charge (SOC). The boundary condition can be in various modes: constant current, constant voltage, constant power, and pulsed power loads, depending on practical applications. The current and voltage conditions can readily be implemented, as done similarly in previous battery models. Simulation of the power boundary condition in the literature was done by using an iterative method in which a guess is taken for the current and a simulation of the cell is carried out to compute the resulting voltage. The voltage is then used to determine an updated current from the given power. The process is repeated until convergence. In the present work, we describe an efficient approach to directly implement the power boundary condition without needing the above-mentioned iterative procedure. Our approach is inspired by the CFD techniques discussed in Ref. [19].
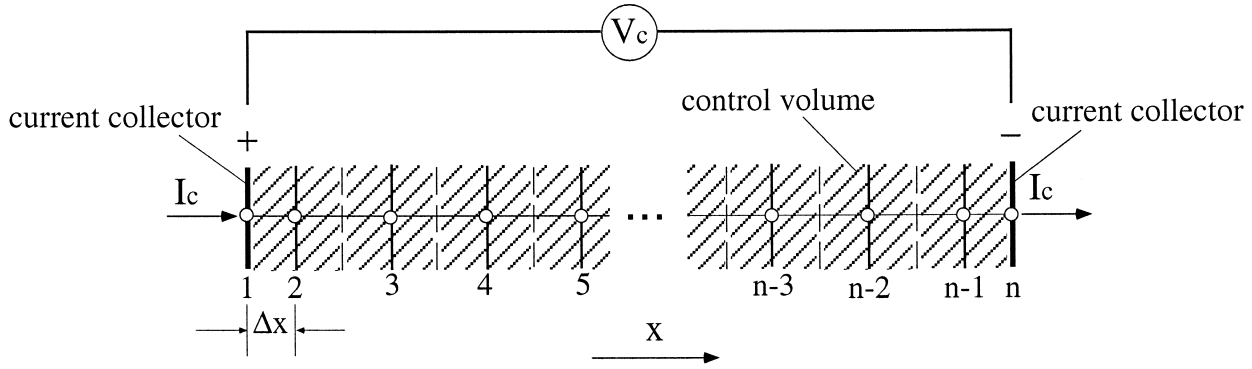
Fig. 3. Schematic of control volumes and computational meshes for a battery cell.

First, the mathematical definition of the current into or out of a cell is given as follows:

$$-\sigma \frac{\partial \phi_s}{\partial x}\bigg|_{x=0} = \frac{I_c}{A_e} \tag{7}$$

where σ is the electrical conductivity of the solid phase, ϕ_s the solid phase potential, x the coordinate defined along the cell width, and A_e the electrode area. Discretize the cell into a number of control volumes as schematically shown in Fig. 3, where 1 starts from the current collector in the positive electrode and n designates the current collector in the negative electrode. The cell voltage V_c is then given by

$$V_c = \phi_s(1) - \phi_s(n) \tag{8}$$

Let $\phi_s(n) = 0$ as the reference potential, and apply the Taylor series expansion to approximate the potential at node 1 in terms of the potential at node 2, Eq. (8) can be recast into

$$V_c = \phi_s(1) = \phi_s(2) - \frac{\partial \phi_s}{\partial x}\bigg|_{x=0} \Delta x \tag{9}$$

where Δx is half the thickness of the control volume adjacent to the current collector in the positive electrode (see Fig. 3). Eliminating $[(\partial \phi_s)/(\partial x)]|_{x=0}$ from Eq. (9) by use of Eq. (7), we have:

$$V_c = \phi_s(2) + \frac{\Delta x}{\sigma A_e} I_c \tag{10}$$

Noting that the cell power is the product of cell current and voltage, and combining Eqs. (3) and (10) gives:

$$\left(C_2 + \frac{\Delta x}{\sigma A_e}\right) I_c^2 + \phi_s(2) I_c - C_1 = 0 \tag{11}$$

Solving Eq. (11) for I_c and substituting it into Eq. (7) yields:

$$-\sigma \frac{\partial \phi_s}{\partial x}\bigg|_{x=0}$$
$$= \frac{-\phi_s(2) + \left[(\phi_s(2))^2 + 4C_1\left(C_2 + \frac{\Delta x}{\sigma A_e}\right)\right]^{1/2}}{2\left(C_2 A_e + \frac{\Delta x}{\sigma}\right)} \tag{12}$$

Eq. (12) is a current flux into the control volume immediately adjacent to the boundary and, thus, can be equivalently implemented as a source term for the control volume around node 2. Its nonlinear dependence upon the potential ϕ_s of the control volume, however, requires a 'linearizing' procedure in order to speed up computations and convergence [19], namely:

$$-\sigma \frac{\partial \phi_s}{\partial x}\bigg|_{x=0} = S_c + S_p \phi_s(2) \tag{13}$$

where S_c stands for the constant part of the current flux, while S_p is the linear coefficient of $\phi_s(2)$. There are different ways to linearize Eq. (12) into the form given by Eq. (13), but S_p must always be negative. Otherwise, a divergent solution or physically unrealistic solutions would arise; see detailed discussion by Patankar [19]. For this reason, we use the following linearization scheme:

$$S_p = -\frac{1}{2\left(C_2 A_e + \frac{\Delta x}{\sigma}\right)} \tag{14}$$

$$S_c = \frac{\left[(\phi_s^o(2))^2 + 4C_1\left(C_2 + \frac{\Delta x}{\sigma A_e}\right)\right]^{1/2}}{2\left(C_2 A_e + \frac{\Delta x}{\sigma}\right)} \tag{15}$$

where ϕ_s^o is the potential value in the previous iteration. Apparently, S_p given by Eq. (14) is always negative.

Table 1
Battery specifications and operating conditions

Battery type	Lead–acid (module) [20]	Ni–MH (single cell) [8]
Cells in series	6	1
Cells in parallel	8	1
Capacity ($C/3$ rate; A h)	85	1.5
Capacity ratio ($-/+$)	1.4	1.5
Dimension of electrode	6.5 in.×6.0 in.	3 in.×3 in.
Electrode area (cm$^{2)}$)	251.6	58.1
Thickness (cm)		
Positive electrode	0.159	0.045[a]
Separator	0.159	0.025
Negative electrode	0.159	0.045[a]
Electrolyte concentration (M)	5.10	7.1
Peak discharge power (W)	3000	4.4[b]
Operating temperature (°C)	23	25

[a]Calculated from the given capacity and capacity ratio.
[b]Calculated from the given maximum current of 4 A.

Numerical tests found that implementation of the power boundary condition using Eq. (13) not only avoids iterating the cell current but also significantly reduces computational time and improves the computational stability.

The general differential Eq. (6) is discretized by the control volume-based finite difference method [19], and the resulting set of linear algebraic equations is iteratively solved. A single numerical solver for the general differential equation is repeatedly applied to each scalar field over a control volume mesh. Furthermore, the present model equations derived from the volume-averaging technique are equally applicable in various regions, such as electrodes, electrolyte reservoir, and separator. Thus, matching conditions between different regions are not necessary. Such a single-domain formulation offers considerable simplifications in numerical simulations. While our simulators are capable of simulating multidimensional behaviors (see,

e.g., [14]), only one-dimensional simulations are needed and carried out in the present work.

Stringent numerical tests were performed in every case to ensure that the solutions were independent of the grid size and time step. For the cases to be illustrated below, it was found that the typical number of grid lines across the cell width was about 60. The equations were solved as a simultaneous set, and the convergence was considered to be reached when the relative error in each field between two consecutive iterations is less than 10^{-6}. A typical DST cycle simulation required approximately 10 min of CPU time for a lead–acid battery and a Ni–MH cell on an HP B160L workstation. In comparison, the real-time testing of the batteries takes 77 min and 3 h, respectively.

2.5. Case studies

While a number of case studies have been performed for various types of batteries and various brands of the same type of batteries, only two batteries are chosen for presentation in this article to demonstrate the unique capability of the integrated simulation and testing approach: a commercially available lead–acid battery and a prototype Ni–MH cell. Other case studies exhibited similar results.

The battery specification and operating conditions for the lead–acid battery and the Ni–MH cell, respectively, are listed in Table 1. Battery-specific parameters are given in Table 2, while kinetic and transport parameters also needed in simulations are taken from Ref. [18] for the lead–acid battery. The Ni–MH cell to be simulated is taken from Ref. [8] along with the experimental data given therein. Since no detail on this cell geometry is given, the electrode thicknesses are estimated from the given capacities with assumed typical electrode capacities given by De Vidts et al. [21] for the MH electrode and De Vidts and

Table 2
Parameters used in simulations

Battery type	Lead–acid (module)	Ni–MH (single cell) [21,22]
Porosity at fully charged state		
Positive electrode	0.61	0.44
Separator	0.92	0.68
Negative electrode	0.55	0.30
Volume fraction of inert material		
PbO$_2$ electrode	0.05	N/A
Pb electrode	0.10	N/A
Radius of active material particles (cm)		
Nickel cylinder (substrate)	N/A	2.9×10^{-4} (1.5×10^{-4})
MH sphere	N/A	10^{-3}
Maximum specific surface area (cm^2/cm^3)		
Positive electrode	2.3×10^5	3864
Negative electrode	2.3×10^4	2100
Electrical resistance (Ω)		
Intercell connector	2×10^{-4}	N/A
Terminal	2×10^{-4}	N/A
Cell grid	2×10^{-3}	N/A

White [22] for the Ni electrode. The sizes of active material particles and other parameters including those of electrode kinetics used in numerical simulations are also taken from their work [21,22].

3. Experimental testing

Experimental testing of the lead–acid battery described in Table 1 was conducted using an AeroVironment ABC-150 battery diagnostic system, and the detailed test procedures were given in Ref. [20] and, thus, not repeated here. The test equipment is versatile and can handle battery modules as well as packs.

4. Results and discussion

4.1. Lead–acid battery

Fig. 4(a) shows both experimental and simulated voltage profiles of the lead–acid battery under the DST cycles. The voltage drops to the lowest point during the 100% peak power discharge and reaches the highest value during 50% peak power charge within each subcycle of 360 s. The difference between the two extremes is about 4 V. Overall, the voltage decreases with the number of subcycles, while it oscillates in phase with the power pulses. The current gradually increases with DOD due to the drop in the battery voltage so that the same power level is main-
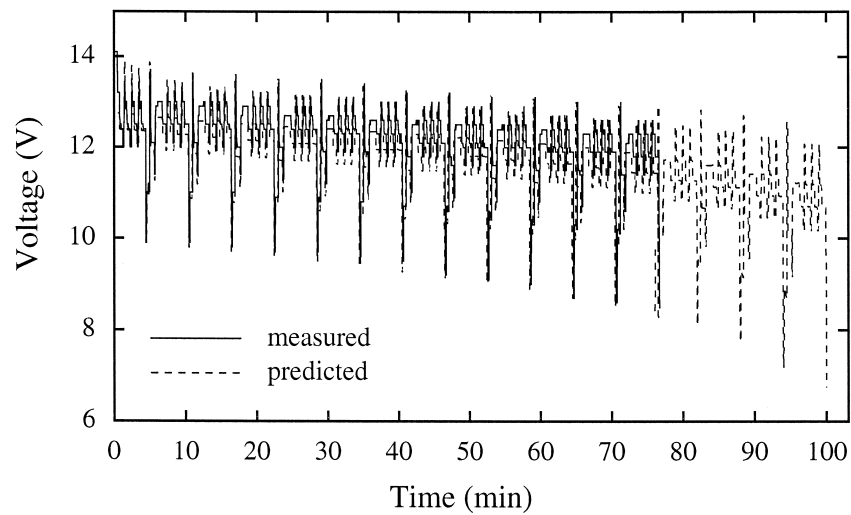
(a) Voltage profile
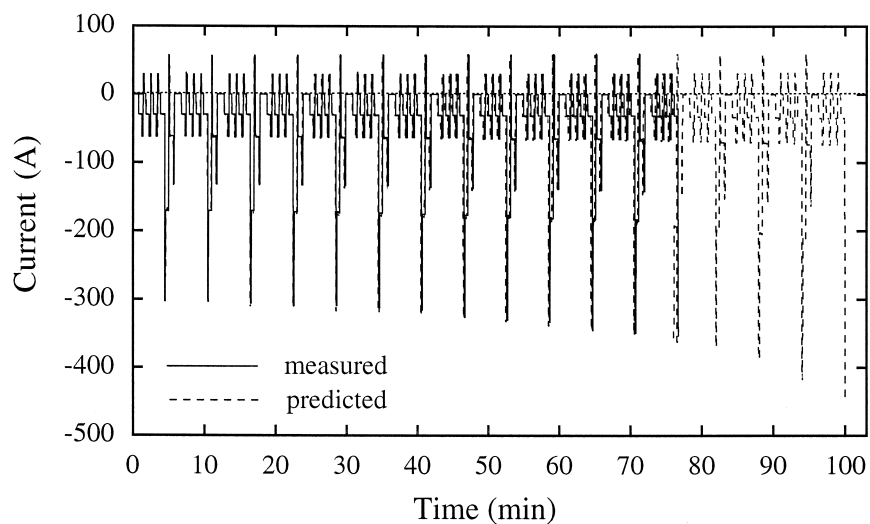
(b) Current profile

Fig. 4. DST curves of the lead–acid battery module at 3.0-kW peak power and ambient temperature. Comparison of the experimental data with simulated results.

tained (see Fig. 4(b)). A good agreement can be seen between the experimental data and simulated results.

More importantly, computer simulations can provide detailed information to understand the battery state in testing. As shown in Fig. 4, the experimental DST cycling is terminated at the 80% DOD in order to avoid battery overdischarge and hence permanent damage. However, the simulation can continue the DST cycling beyond the 80% DOD up to a point when the battery is fully discharged (at $t \approx 100$ min). This information permits us to determine the limit of the battery under the DST cycle or in a real driving cycle in a nondestructive fashion.

Fig. 5 shows the electrolyte concentration distributions across the lead–acid cell at the end of the experimental and simulated DST cycles, respectively. At the end of the laboratory testing (solid line), the acid concentration exhibits a nonuniform profile, but there is still a sufficient amount of acid inside the battery cell for further discharge. However, the acid concentration at the end of the simulated DST cycle (dotted line) is virtually zero at the positive electrode, thus causing a drastic drop in the cell voltage. There also exists a sharp decrease of the acid concentration at the interface between the positive electrode and the separator. This is because the local porosity is smallest corresponding to the largest active material utilization (see Fig. 6) and the acid transport from the separator to the positive electrode is somewhat choked. It appears beneficial for the lead–acid battery to increase its initial porosity of the positive electrode as much as practically possible.

The simulator can also provide data that cannot be easily measured during the battery testing. For instance, the local state of charge, which reflects the active material utilization, is a key parameter to evaluate battery performance under a certain duty. Unfortunately, it is difficult to measure. In contrast, a simulator based on first principles can generate such information concurrently with the volt-

Fig. 6. Electrode active material utilization profiles across the lead–acid cell at $t = 76.06$ min (corresponding to the end of the DST cycle testing) and $t = 99.97$ min (at the end of the simulated DST cycle).

age and current profiles. Therefore, additional information can be offered by the simulation to help evaluate the battery performance.

Fig. 6 displays the active material utilization profiles in both electrodes of the lead–acid cell at the end of testing and simulation, respectively. The active material utilization here is defined by the percentage of the maximum charge capacity as determined by comparing the amount of active material participating in the electrode reaction to the initial amount. It can be seen that the active material utilization distribution is severely nonuniform at the positive electrode at the end of the DST cycle testing, with the active material near the interface between the positive electrode and the separator being almost used up. The utilization of active material at the negative electrode generally remains low, indicating that a large amount of active material at the negative electrode is unused. This result shows that for the simulated driving cycle, the capacity of the negative electrode is overdesigned. It should be possible to increase the specific energy of the lead–acid battery simply by reducing the size and hence weight of the negative electrode. In general, Fig. 6 reveals that the tested lead–acid battery underutilized the active material by as much as 70% under the simulated EV duty, indicating great potential of increasing the specific energy of the lead–acid battery and reducing the cost through the simulation-based design.

4.2. Ni–MH cell

The DST cycle curves for the Ni–MH cell produced by experiment and simulation are shown in Fig. 7. The general shape of the voltage curves is similar to that of the lead–acid battery, except for the initial quick drop which may be attributed to the hydrogen absorption–adsorption equilibrium inside the MH particles. The equilibrium or open-circuit potential of intercalative cells, such as Ni–MH and Li-ion is strongly dependent upon the local state of
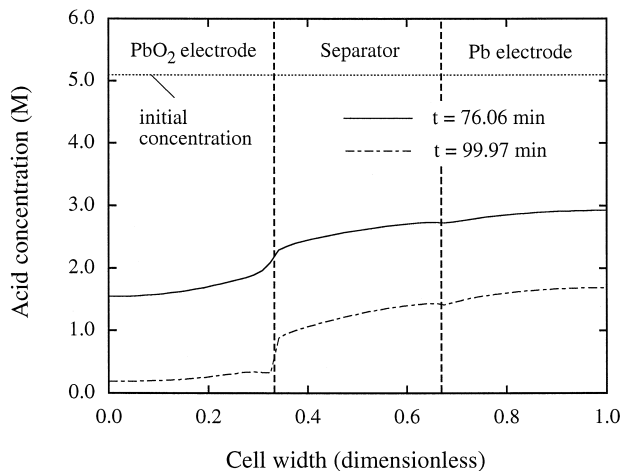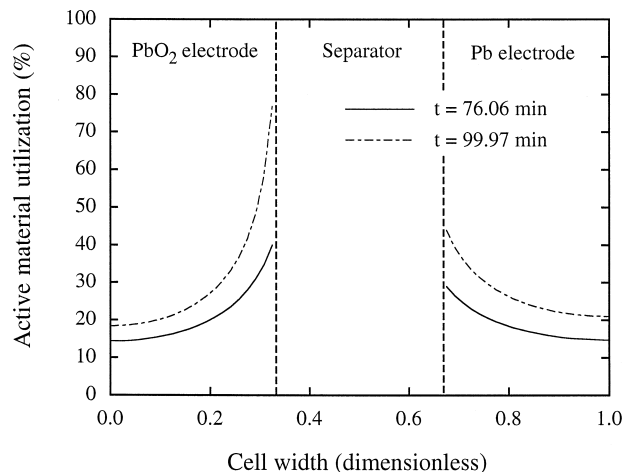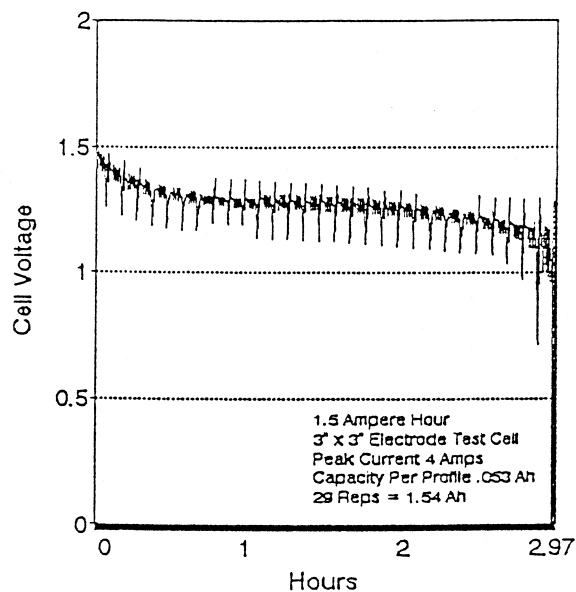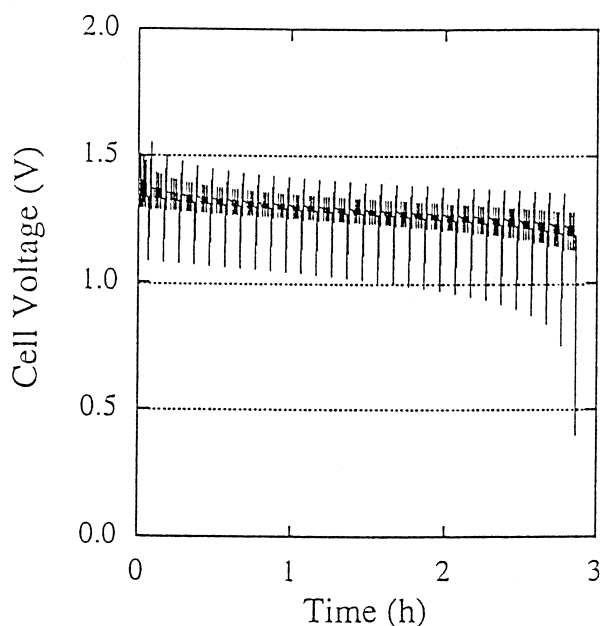

Fig. 5. Electrolyte concentration profiles across a lead–acid battery cell at $t = 76.06$ min (corresponding to the end of the DST cycle testing) and $t = 99.97$ min (at the end of the simulated DST cycle).

(a) Measured [8]

(b) Simulated

Fig. 7. Comparison of measured and simulated DST voltage profiles of a Ni–MH cell.

charge. More specifically, it is a function of the surface concentration of reactant species. However, such thermodynamic information is not available for the studied cell and, thus, this dependence is not included in the present simulation. Nevertheless, a qualitative comparison between experimental and predicted data can be made and a reasonable agreement is seen in Fig. 7. In particular, the end of the DST cycle was measured at 2.97 h vs. predicted at 2.87 h. Some discrepancies between the measured and simu-

lated voltages, as can be observed in Fig. 7, may possibly be reduced if the input parameters are all given.

Fig. 8 shows the predicted proton and hydrogen concentration profiles across the Ni–MH cell during the DST cycle. The cell voltage drops very quickly at the end of DST simulation, which indicates the exhaust of the active material at the reaction site (i.e., the electrode/electrolyte interface). The proton concentration reaches the maximum value at the surface of Ni active material so that the cell can no longer be discharged, while the average proton concentration within the active material particles are still below the maximum value meaning more capacity available to incorporate protons and hence discharge. Therefore, the performance of this Ni–MH cell is dictated by the microscopic proton diffusion from the surface to the bulk of NiOOH particles. The availability of the active material at the surface of MH particles is also strongly dependent on the hydrogen diffusion from the bulk to the surface as the surface hydrogen concentration continually diminishes with discharge. The departure of the interfacial from the bulk concentrations in microscopic particles is proportional to the transfer current density produced at the reaction interface. As the battery goes deeper in DOD and withdraws a larger current under the constant-power discharge, the difference between the bulk and interfacial concentrations becomes larger and reaches the maximum at the end of the DST cycle. This maximum difference could be used to identify the limiting mechanisms for the operation of a specific cell.

Because the capacity ratio of the MH electrode over the Ni electrode was designed to be 1.5 [8], this Ni–MH cell is positive electrode limiting. It can be seen from Fig. 8 that there is still plenty of hydrogen (ca. 40%) available in the bulk of the MH particles at the end of the DST cycle. Because the MH material is expensive, one may design a more compact and economical Ni–MH cell without degrading the performance.
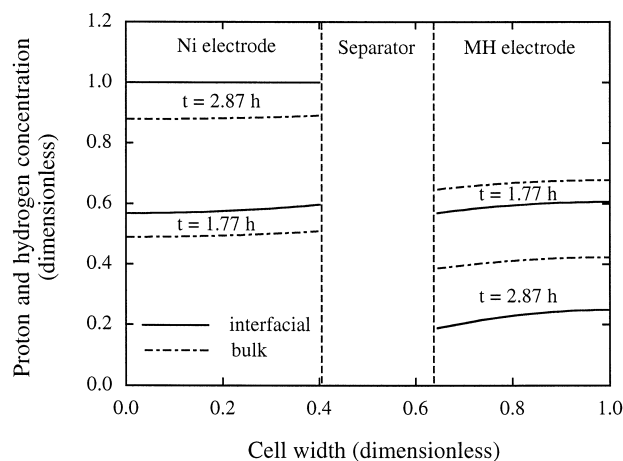

Fig. 8. Predicted proton and hydrogen concentration profiles across the Ni–MH cell during the DST cycle at $t = 1.77$ h (corresponding to the cutoff voltage of 1.0 V) and $t = 2.87$ h (when the cell voltage drops below 0.4 V).
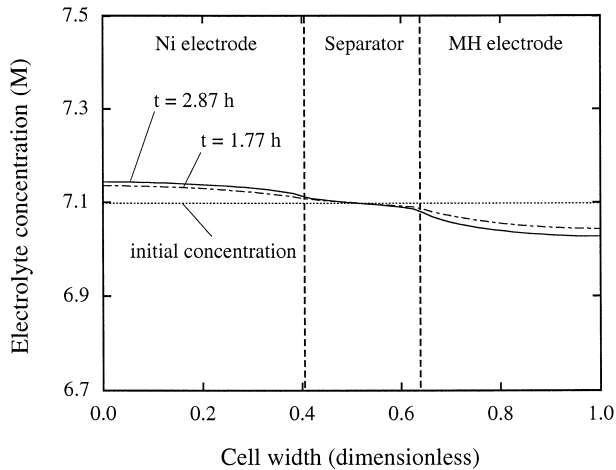
Fig. 9. Simulated electrolyte concentration profiles across the Ni–MH cell during the DST cycle at $t = 1.77$ h (corresponding to the cutoff voltage of 1.0 V) and $t = 2.87$ h (when the cell voltage drops below 0.4 V).

Unlike the lead–acid battery which is limited by the depletion of acid at the positive electrode, the electrolyte concentration in Ni–MH batteries has little effect on the performance. During discharge, the alkaline is produced at the Ni electrode and consumed at the MH electrode. The total alkaline is, however, conserved during battery operation. In addition, in the DST cycle a discharge pulse is followed immediately by a rest period and/or a charge pulse, therefore, the electrolyte concentration distribution across the cell is expected to be more uniform than in a constant load discharge. Fig. 9 shows that the alkaline concentration is indeed close to the initial value during the DST cycle and does not become a limiting factor for the performance of the Ni–MH cell.

5. Conclusions

An integrated simulation and testing approach is demonstrated for the evaluation of EV batteries. This novel approach combines state-of-the-art battery simulators and test facilities to yield valuable information that enables innovative battery design and improvement.

The developed computer simulators are capable of dealing with various charge and discharge regimes, including the power-based test regimes like the DST and SFUDS cycles. Comparisons were made between the simulation results and the experimental data for a commercially available lead–acid battery and a prototype Ni–MH cell. Good agreement was obtained between the measured and simulated voltage curves under the DST cycle. Moreover, simulated results reveal the potential of increasing specific energy and reducing costs as well as the areas for design improvements. Here lies the significance of this integrated simulation and testing approach.

Thermal effects during a simulated or actual driving cycle can be important to the battery performance. For the case of the lead–acid batteries, the temperature rise within the driving cycle may result in the loss in capacity [23] and, hence, the reduction of cycle life. The high thermal stresses imposed by the driving cycle will be incorporated in our simulators in the future work.

6. List of symbols

A_e	electrode area (cm^2)
C_1, C_2	coefficients introduced in Eqs. (4) and (5)
I	current (A)
N	number of cells
P	power (W)
R	electrical resistance (Ω)
S	source term
t	time (s)
V	voltage (V)
v	velocity vector (cm/s)
x	coordinate in the direction of cell width (cm)

Greek symbols

Γ	diffusion coefficient (cm^2/s)
Δx	half thickness of a control volume along x-direction (cm)
σ	electronic conductivity of the solid matrix (S/cm)
ϕ_s	electric potential in the solid active material phase (V)
Φ	a general variable in Eq. (6)

Subscripts

b	battery
c	cell
g	grid
ic	intercell connector
p	cells in parallel
s	cells in series
t	terminal

Acknowledgements

References

[1] B.E. Dickinson, D.H. Swan, T.R. Lalk, Comparison of advanced battery technologies for electric vehicles, in: Electric Vehicle Power Systems—Hybrids/Batteries/Fuel Cells, SAE SP-984 (1993) 1–11.
[2] EHP Battery Test Working Task Force, USDOE, Report No. DOE/ID 10146, Aug. 1988.

[3] G. Hunt, USABC Electric Vehicle Battery Test Procedures Manual, Rev. 2, USABC, Jan. 1996.

[4] D.D. Brandt, Driving cycle testing of electric vehicle batteries and systems, J. Power Sources 40 (1992) 73–79.

[5] K.A. Striebel, F.R. McLarnon, E.J. Cairns, Laboratory-scale evaluation of secondary alkaline zinc batteries for electric vehicles, J. Power Sources 47 (1994) 1–11.

[6] A.F. Hollenkamp, L.T. Lam, C.G. Phyland, N.C. Wilson, Evaluation of lead/acid batteries under simulated electric-vehicle duty: development of design parameters on the basis of SFUDS performance, J. Power Sources 59 (1996) 177–183.

[7] N. Ito, H. Inoue, K. Sato, N. Morishita, M. Ikoma, Development of sealed-type nickel/metal-hydride battery for electric vehicle, EVS 13 (1996) 31–36.

[8] D.E. Reisner, J.H. Cole, M. Klein, Bipolar nickel–metal hydride EV battery, EVS 13 (1996) 37–44.

[9] W. Tiedemann, J. Newman, Mathematical modeling of phenomena contributing to thermal rise in lead–acid batteries used in electric vehicles, in: K.R. Bullock, D. Pavlov (Eds.), Advances in Lead–Acid Batteries, PV 84-14 (1984) 336–347.

[10] P. Ekdunge, Simplified model for the lead–acid battery, J. Power Sources 46 (1993) 251–262.

[11] Y. Chen, J.W. Evans, Three-dimensional thermal modeling of lithium–polymer batteries under galvanostatic discharge and dynamic power profile, J. Electrochem. Soc. 141 (1994) 2947–2955.

[12] M. Doyle, J. Newman, The use of mathematical modeling in the design of lithium/polymer battery systems, Electrochim. Acta 40 (1995) 2191–2196.

[13] E. Karden, P. Mauracher, F. Schope, Electrochemical modeling of lead/acid batteries under operating conditions of electric vehicles, J. Power Sources 64 (1997) 175–180.

[14] W.B. Gu, C.Y. Wang, B.Y. Liaw, Numerical modeling of coupled electrochemical and transport processes in lead–acid batteries, J. Electrochem. Soc. 144 (1997) 2053–2061.

[15] B.Y. Liaw, W.B. Gu, C.Y. Wang, Numerical simulation of coupled electrochemical and transport processes in battery system, Paper No. 97124, in: Proceedings of 32nd Intersociety Energy Conversion Engineering Conference, SAE, Warrendale, PA, 1997.

[16] C.Y. Wang, W.B. Gu, B.Y. Liaw, Micro-macroscopic coupled modeling of batteries and fuel cells: Part 1. Model development, J. Electrochem. Soc. (1998) in press.

[17] W.B. Gu, C.Y. Wang, B.Y. Liaw, Micro-macroscopic coupled modeling of batteries and fuel cells: Part 2. Application to Ni–Cd and Ni–MH cells, J. Electrochem. Soc. (1998) in press.

[18] T.V. Nguyen, R.E. White, H. Gu, The effect of separator design on the discharge performance of a starved lead–acid cell, J. Electrochem. Soc. 137 (1990) 2998–3004.

[19] S.V. Patankar, Numerical Heat Transfer and Fluid Flow, Hemisphere, Washington, DC, 1980.

[20] M. Geng, B.Y. Liaw, Test Report HBTL-004, Hawaii Battery Testing Laboratory, 1997.

[21] P. De Vidts, J. Delgado, R.E. White, Mathematical modeling for the discharge of a metal hydride electrode, J. Electrochem. Soc. 142 (1995) 4006–4013.

[22] P. De Vidts, R.E. White, Mathematical modeling of a nickel–cadmium cell: proton diffusion in the nickel electrode, J. Electrochem. Soc. 142 (1995) 1509–1519.

[23] B.L. McKinney, G.H. Brilmyer, The impact of urban driving schedules on the thermal management of lead–acid batteries for electric vehicles, in: K.R. Bullock, D. Pavlov (Eds.), Advances in Lead–Acid Batteries, PV 84-14 (1984) 348–359.